Higher-dimensional generalization of the Kitaev spin liquid

Po-Jui Chen [1,*] and Piers Coleman [1,2]

[1]*Department of Physics and Astronomy, Rutgers University, Piscataway, New Jersey 08854, USA*

[2]*Department of Physics, Royal Holloway University of London, Egham, Surrey TW20 0EX, United Kingdom*

(Received 17 June 2025; revised 22 October 2025; accepted 19 March 2026; published 20 April 2026)

We construct an exactly solvable model of a four-dimensional Kitaev spin liquid. The lattice structure is orthorhombic and each unit cell contains six sublattice degrees of freedom. We demonstrate that the Fermi surface of the model is made up of two-dimensional surfaces. Additionally, we evaluate the energy cost of creating visons using scattering theory. The positive bond-flip energy suggests that the flux-free state is locally stable. Our model sheds light on the realization of high-dimensional fractionalization.

DOI: 10.1103/fvjg-pb5k

I. INTRODUCTION

The quantum spin liquid is an exotic phase of matter which lacks long-range magnetic order and does not exhibit any broken symmetry. Instead, the ground state of a spin liquid is characterized by its long-range quantum entanglement [1–5]. Another useful way to understand quantum spin liquids is in terms of their elementary excitations. The low-energy effective field theory for quantum spin liquids often involves fractionalized spin excitations moving under an emergent gauge field. Here, fractionalization refers to the phenomenon whereby elementary excitations carry fractional quantum numbers: typical examples include neutral spin 1/2 spinons, and spinless visons, which describe excitations of the gauge fields. Although quantum spin liquids provide a new venue for physicists to explore quantum materials and solve fundamental problems in strong correlation physics, it is a challenge to discover exactly solvable models that can be used as platforms for studying quantum spin liquids. One of the great innovations in this respect is Kitaev's exactly solvable honeycomb model [6], which consists of bond-dependent Ising interactions between spin-1/2 local moments. Kitaev's decomposition reveals the underlying physics of spins, fractionalized into Majorana fermions moving through a static Z_2 gauge field. The defects of the Z_2 gauge field are plaquette fluxes, called visons. Kitaev's model demonstrated that the transition between gapless and gapped topological phases is driven by tuning the strengths of the spin coupling constants. The gapped phases of the Kitaev honeycomb model support the existence of non-Abelian anyons of possible interest to topological quantum computation [7,8]. Since the original work by Kitaev, many exactly solvable three-dimensional variants of the original model have been studied [9–15], classified through their topology and the presence of gapless Dirac cones, or Fermi surfaces in the excitation spectrum [12,16]. There are also several theoretical proposals which extend the Kitaev model by introducing an additional orbital degree of freedom [17–19].

On the experimental side, several experiments have sought the realization of the Kitaev spin liquid in materials with strong spin-orbit coupling [11,20–22]. α-$RuCl_3$ and iridates [20,23] are candidates for Kitaev materials, in which the interplay between strong correlation in d electrons and spin-orbit coupling gives rise to the anisotropic Ising interaction. In these Kitaev materials, inelastic neutron scattering [24] and Raman scattering [19,25,26] have revealed tentative signatures of spin fractionalization in these materials.

On the other hand, there has been a revival of interest in high-dimensional physics. In particular, the four-dimensional quantum Hall state [27], topological Anderson insulator [28], Floquet topological insulator [29], and five-dimensional Weyl semimetals [30,31] have been subjects of theoretical investigation. Experimentally, atomic systems [32], photonic platforms [33,34], and specially designed quantum circuits [35,36] have been proposed to simulate 4D physics. These experimental advances provide an additional motivation for studies of higher-dimensional physics.

In an effort to gain further insight into Kitaev spin liquids and high-dimensional physics, here we introduce a four-dimensional realization, a natural generalization of the 2D and 3D Kitaev spin liquids, as shown in Figs. 1(a) and 1(b), which we call the hyperhexagonal lattice. The key structural motif in our model is a chain of alternating xx and yy bonds, which we then wrap around an even-sided helix, to form a structure with an even number of $2n$ atoms per unit cell, as shown in Fig. 1. We then add zz bonds as cross-links between the helices. Thus, the 2D honeycomb model consists of zigzag chains, connected by zz cross-links. For $n = 2$, we create a four-sided helix with four atoms per unit cell, forming the three-dimensional "hyperoctagonal" lattice [10]. Generalizing this procedure, for a $2n$-sided helix we form a structure with cross-links in n independent directions, which together

*Contact author: pc863@physics.rutgers.edu

Published by the American Physical Society under the terms of the Creative Commons Attribution 4.0 International license. Further distribution of this work must maintain attribution to the author(s) and the published article's title, journal citation, and DOI.

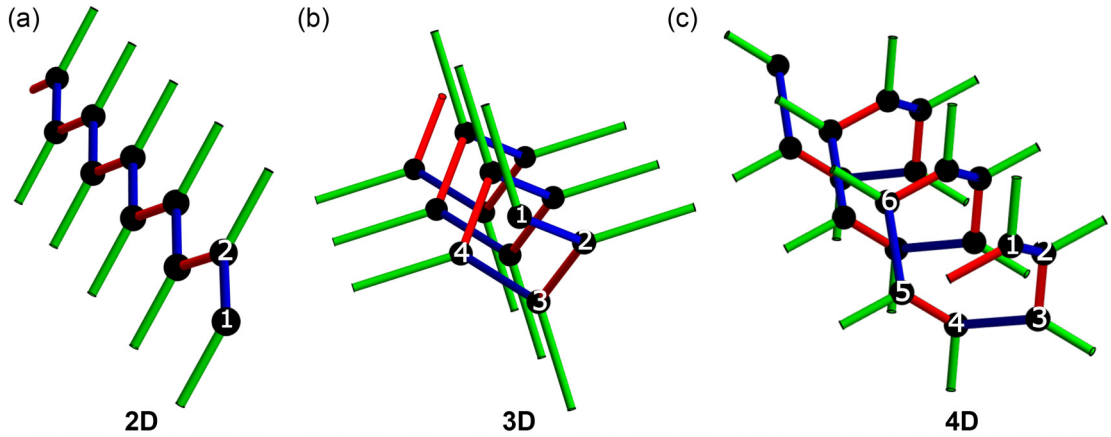


FIG. 1. The dimensional evolution of spiral Kitaev models. (a) The honeycomb represented as a 2D flattened spiral, (b) the 3D hyperoctagon, and (c) the 4D hyperhexagon, illustrated in three dimensions by projecting out the $\hat{n} = (1, 1, 1, 0)$ direction. The blue-red bonds denote the alternating xx, yy chain, while the green zz bonds link the spirals.

with the axis of the helix forms a $D = n + 1$ dimensional structure. Thus, for $n = 3$, we form a six-sided helix with a hexagonal cross-section embedded in $D = 4$ dimensions—the "hyperhexagon". To visualize this novel structure, we project it into the three-dimensional hyperplane perpendicular to the $\hat{n} = (1, 1, 1, 0)$ direction: viewed along the axis of the helix, it then forms a hexagonal structure in which the xx-yy chain wraps around the hexagon as one proceeds along the fourth w axis, (0,0,0,1) as shown in Fig. 1(c).

With this lattice geometry, we can perform a spin-fermionization in four dimensions, formally identical to those in two and three dimensions. The resulting physics describes a free Majorana fermion moving on a four-dimensional lattice containing six sites per unit cell. Its exact solvability enables us to investigate its energy spectrum, ground state, and elementary excitations.

The remaining discussion is organized as follows. Section II describes the lattice geometry of the four-dimensional Kitaev spin liquid, including its Hamiltonian, and Wilson loop operators. In Sec. III, we compute the energy spectrum for the isotropic case and demonstrate that the Fermi surface of excitations is two dimensional, embedded in a four-dimensional manifold. In Sec. IV, we discuss the vison gap of our model and argue that the system is locally stable against gauge excitations. Section V discusses the validity of the Jordan-Wigner transformation for the four-dimensional model, the possibility of arbitrary dimensional extensions.

II. THE MODEL AND ITS SPIN-FERMIONIZATION

The Kitaev spin model

$$H_K = \sum_{\langle i,j \rangle} J_{\alpha_{ij}} \sigma_i^{\alpha_{ij}} \sigma_j^{\alpha_{ij}}, \tag{1}$$

where $\langle ij \rangle$ denotes neighboring sites on the lattice and α_{ij} identifies the type of bond (xx, yy, zz), can be embedded on any lattice with threefold coordination that can be consistently tiled with x, y, or z bonds. Its extension to four dimensions requires that we now construct such a lattice.

We begin by introducing the detailed helical spatial structure for our four-dimensional spin liquid, which we call the hyperhexagonal lattice. To this end, we consider an orthorhombic lattice with six lattice points in one unit cell, as shown in Fig. 2. We take our four-dimensional basis to be $\hat{\mathbf{x}} = (1, 0, 0, 0)$, $\hat{\mathbf{y}} = (0, 1, 0, 0)$, $\hat{\mathbf{z}} = (0, 0, 1, 0)$, and $\hat{\mathbf{w}} = (0, 0, 0, 1)$. To display the structure, we have projected it into the two-dimensional plane perpendicular to the $\hat{\mathbf{w}}$ and $\mathbf{n} = (1, 1, 1, 0)$ directions. The projected $\hat{\mathbf{x}}$, $\hat{\mathbf{y}}$, and $\hat{\mathbf{z}}$ directions are shown as a right-angled coordinate system, such that $\hat{\mathbf{n}}$ is perpendicular to the plane of the paper. We label the six sites in the unit cell by $i = 1, 2, \ldots, 6$. Each site is connected to its nearest neighbors at $i' = (i \pm 1) \mathrm{mod} 6$. On the other hand, each unit cell is connected to its six neighbors as shown in Fig. 2, and labeled by green bonds, which enables the

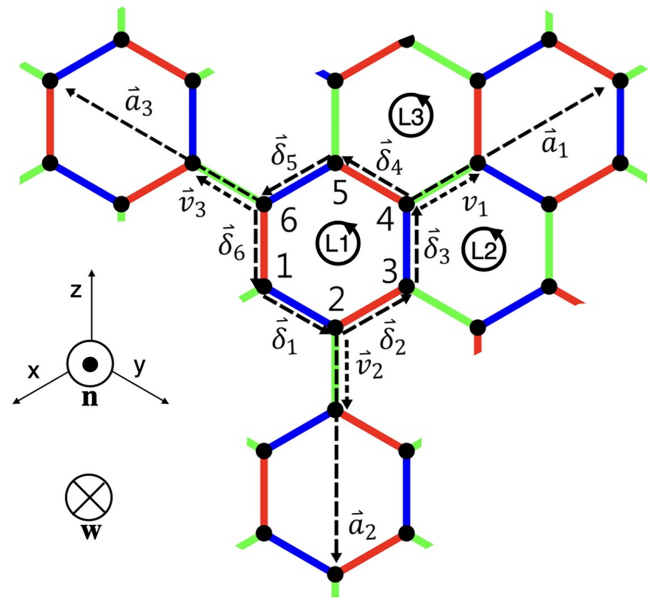


FIG. 2. (a) The projected lattice structure of our 4D Kitaev spin liquid. The figure is obtained by first projecting along the w direction and then projecting along the $\mathbf{n} = (1, 1, 1, 0)$ direction. (b) Three fundamental plaquette operators for the 4D Kitaev spin liquid. There are 12 or 14 bonds in a fundamental loop. Emitter and Absorber specify the sign arrangement of a loop for the flux-free configuration.

lattice structure to expand in the x, y, z, linking direction. From Fig. 2, site i links to site $(i+3)\mathrm{mod}(6)$ in neighboring unit cells, i.e., 1 is connected to 3, 2 to 5, and 3 to 6 by the green intercell links.

The geometric structure within a unit cell is described by vectors $\boldsymbol{\delta_i} = \boldsymbol{x}_{i+1} - \boldsymbol{x}_i$, $(i = 1, 6)$, where $\boldsymbol{x_i}$ denotes the position of atoms sitting inside the unit cell and

$$\begin{aligned} \boldsymbol{\delta_1} &= \hat{\mathbf{y}} + \mathbf{w}\,, \quad & \boldsymbol{\delta_4} &= -\hat{\mathbf{y}} \\ \boldsymbol{\delta_3} &= \hat{\mathbf{z}} + \mathbf{w}\,, \quad & \boldsymbol{\delta_6} &= -\hat{\mathbf{z}} \\ \boldsymbol{\delta_5} &= \hat{\mathbf{x}} + \mathbf{w}\,, \quad & \boldsymbol{\delta_2} &= -\hat{\mathbf{x}}. \end{aligned} \tag{2}$$

With this choice of lattice vectors, the pitch of the spiral is three units in the w direction. The vectors representing the green bonds linking the unit cells are

$$\begin{aligned} \boldsymbol{v_1} &= \tfrac{1}{2}\mathbf{n} - \hat{\mathbf{x}}, \quad \boldsymbol{v_2} = \tfrac{1}{2}\mathbf{n} - \hat{\mathbf{z}}, \\ \boldsymbol{v_3} &= \tfrac{1}{2}\mathbf{n} - \hat{\mathbf{y}}. \end{aligned} \tag{3}$$

Notice how even-numbered bonds $\boldsymbol{\delta_i}$, $(i = 2, 4, 6)$ and cross-links $\boldsymbol{v_i}$ $(i = 1, 3)$ do not advance in the w direction. This choice has been chosen to guarantee that passage around any hexagonal loop in the structure increments the w coordinate by a multiple of 3, leading to a closed structure.

The positions of unit cells are described by the following primitive lattice vectors:

$$\begin{aligned} \boldsymbol{a_1} &= \left(\tfrac{-3}{2}, \tfrac{3}{2}, \tfrac{3}{2}, 2\right), \\ \boldsymbol{a_2} &= \left(\tfrac{3}{2}, \tfrac{3}{2}, \tfrac{-3}{2}, -1\right), \\ \boldsymbol{a_3} &= \left(\tfrac{3}{2}, \tfrac{-3}{2}, \tfrac{3}{2}, 2\right), \\ \boldsymbol{a_4} &= (0, 0, 0, 3). \end{aligned} \tag{4}$$

Note that $\mathbf{a}_1 + \mathbf{a}_2 + \mathbf{a}_3 - \mathbf{a}_4 = \frac{3}{2}\mathbf{n}$, so we could have also chosen $\frac{3}{2}\mathbf{n}$ as a lattice vector.

Consistency requires that after passage around a closed loop in the projected 2D space, as shown in Fig. 2, the final coordinate $\boldsymbol{x_f}$ either coincides with the initial point $\boldsymbol{x_i}$ or a point that is shifted by a Bravais lattice vector, i.e., $\boldsymbol{x_f} - \boldsymbol{x_i} = \sum_j n_j \boldsymbol{a_j}$, with $n_j \in \mathbb{Z}$. In particular, we note that advancing anticlockwise around the primary hexagonal loop (L1 in Fig. 2), gives a pitch of $\circlearrowleft_1 = \sum_i \boldsymbol{\delta}_i = \mathbf{a}_4$ while advancing around the secondary loop L2 gives $\sum_{\circlearrowleft_2} = -(\boldsymbol{\delta_1} + \boldsymbol{\delta_3} + \boldsymbol{\delta_5} + \boldsymbol{v_1} + \boldsymbol{v_2} + \boldsymbol{v_3}) = -\frac{3}{2}\mathbf{n} - \mathbf{a_4}$ and $\sum_{\circlearrowleft_3} = \boldsymbol{v_1} + \boldsymbol{v_2} + \boldsymbol{v_3} - (\boldsymbol{\delta_2} + \boldsymbol{\delta_4} + \boldsymbol{\delta_6}) = \frac{3}{2}\mathbf{n}$.

Having identified the Bravais lattice vectors, we can determine the volume of the unit cell

$$\Omega_{4D} = \epsilon^{\alpha\beta\gamma\delta} a_1^\alpha a_2^\beta a_3^\gamma a_4{}^\delta = \frac{81}{2}, \tag{5}$$

and the corresponding corresponding reciprocal lattice vectors, normalized so that $\mathbf{b}_a \cdot \mathbf{a}_b = \delta_{ab}$, determined from $\mathbf{b_1}^\alpha = \frac{1}{\Omega_{4D}} \epsilon^{\alpha\beta\gamma\delta} a_2^\beta a_3^\gamma a_4{}^\delta$ and cyclic permutations, which gives

$$\begin{aligned} \mathbf{b_1} &= \left(0, \tfrac{1}{3}, \tfrac{1}{3}, 0\right), \\ \mathbf{b_2} &= \left(\tfrac{1}{3}, \tfrac{1}{3}, 0, 0\right), \\ \mathbf{b_3} &= \left(\tfrac{1}{3}, 0, \tfrac{1}{3}, 0\right), \\ \mathbf{b_4} &= \left(-\tfrac{1}{9}, -\tfrac{1}{9}, -\tfrac{4}{9}, \tfrac{1}{3}\right). \end{aligned} \tag{6}$$

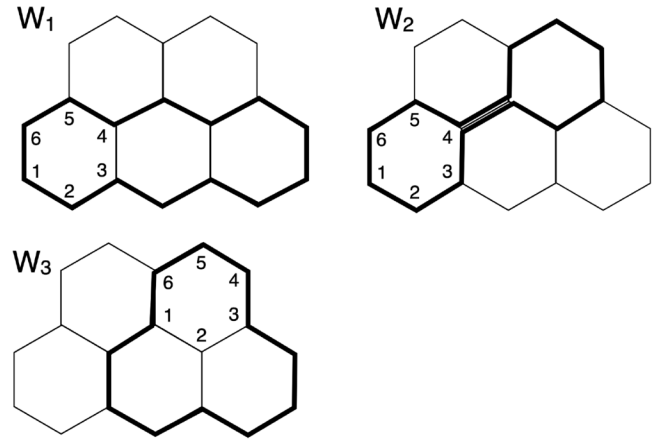


FIG. 3. Three fundamental Wilson loops for the 4D Kitaev spin liquid. There are 12 or 14 bonds in a fundamental loop. Note that $W_1 W_2 = W_3$.

It is convenient to resolve the momentum in reciprocal space $\mathbf{k} = \sum_{\alpha=1,4} k_\alpha \mathrm{b}_\alpha$, where the components are then given by $k_\alpha = \mathbf{k} \cdot \mathrm{a}_\alpha$.

Majorana representation

Here, we briefly review the application of Kitaev's method to the hyperhexagon. The central idea of Kitaev's method is to fractionalize spins into Majorana fermions, according to $\sigma_i^\alpha = 2ic_j b_j^\alpha$, where c_j, b_j^α are Majorana operators whose particles are their own antiparticle $c_j = c_j^\dagger, b_j^\alpha = b_j^{\alpha\dagger}$. These operators also obey the commutation relations $\{c_i, c_j\} = \delta_{ij}$, $\{b_i^\alpha, b_j^\beta\} = \delta_{\alpha,\beta}\delta_{i,j}$, $\{c_i, b_j^\alpha\} = 0$. One should notice that when spin operators are replaced as a product of Majorana operators, the local Hilbert space of the system is expanded, necessitating a projection into the physical subspace through the constraint $D_j = 4ic_j b_j^x b_j^y b_j^z = 1$. After this substitution, the resulting Hamiltonian becomes

$$H_K = \sum J_{\alpha_{ij}} u_{ij} (2ic_i c_j), \tag{7}$$

where $u_{ij} = -2ib_i^{\alpha_{ij}} b_j^{\alpha_{ij}}$ satisfies the unitary condition $u_{ij}^2 = 1$. If we exchange the index i, j, the operator picks up a minus sign $u_{ij} = -u_{ji}$. This factor characterizes the emergent Z_2 gauge symmetry under the transformation $c_i \to Z_i c_i$, $u_{ij} \to Z_i u_{ij} Z_j$. Another important aspect of this model is its conserved quantities. We can find the fundamental Wilson loop operators that commute with the Hamiltonian. In the hyperhexagon, these loops are 12 or 14 lattice constants long, as shown in Fig. 3. The loop operators are products of Pauli matrices along the selected path.

$$W_p = \prod_{i \in \text{loop } p} \sigma_i^{\alpha_i}, \tag{8}$$

where i denotes the site index while the component $\alpha_i \in [x, y, z]$ is chosen from the bond external to the loop at site i (so $\alpha_i \neq \alpha_{i,i+1}, \alpha_{i-1,i}$). As in the hyperoctagon, these loops are not independent of each other [10], satisfying $W_3 = W_1 W_2$.

Both operators are constants of motion since $[W_p, H] = 0$. In terms of the Majorana language, they can be rewritten as $W_p = \prod_{\langle ij\rangle\in\text{loop}} u_{ij}$. The loop operators square to unity, with eigenvalues ± 1, corresponding to a Z_2 flux. In what follows, we provide the guiding rule of gauge choice on bonds u_{ij} such that the system is flux-free. Our construction relies on the definition of emitter and absorber, corresponding to odd and even numbered sites, respectively. On the fundamental loops, we specify a flux-free configuration (all W_p s are 1) by assigning an alternating emitter-absorber arrangement. With this pattern, we define the ordered bond variables as follows:

$$u_{\langle ij\rangle} = \begin{cases} u_{ij}, & \text{if } i \text{ is odd} \\ u_{ji}, & \text{if } j \text{ is odd} \end{cases}. \tag{9}$$

With this definition, we can express the loop operators as $\prod_{\langle ij\rangle\in\text{loop}} u_{\langle ij\rangle}$ the gauge choice for the flux-free sector is $u_{\langle ij\rangle} = 1$ for all $\langle ij\rangle$ pairs.

III. MAJORANA BAND STRUCTURE

A. Energy spectrum

We are now in a position to rewrite the gauge-fixed Hamiltonian in momentum space. We first transform the Majorana fermions into momentum space operators $c_{\alpha,\mathbf{k}} = \frac{1}{\sqrt{N}}\sum_j e^{-i\mathbf{k}\cdot\boldsymbol{R}_j} c_{\alpha,j}$, where $\alpha = (1, 2, \ldots, 6)$ denotes the sublattice index, $\mathbf{k}$ is the momentum and $\mathbf{R}_i$ denotes the location of the unit cell. The momentum space operators $c_{\alpha,\mathbf{k}}$ behave as canonical complex fermions, namely $\{c_{\alpha,\mathbf{k}}, c^\dagger_{\beta,\mathbf{k}'}\} = \delta_{\alpha\beta}\delta_{\mathbf{k},\mathbf{k}'}$, however, they are not independent in the two halves of momentum space, since $c^\dagger_{\alpha,\mathbf{k}} = c_{\alpha,-\mathbf{k}}$. We can then write the Hamiltonian as

$$H = \sum_{\mathbf{k}\in\frac{1}{2}\text{BZ}} c^\dagger_{\mathbf{k}} h(\mathbf{k}) c_{\mathbf{k}}, \tag{10}$$

where $c^\dagger_{\mathbf{k}} = (c^\dagger_{1\mathbf{k}}, c^\dagger_{2\mathbf{k}}, c^\dagger_{3\mathbf{k}}, c^\dagger_{4\mathbf{k}}, c^\dagger_{5\mathbf{k}}, c^\dagger_{6\mathbf{k}})$ and the sum over momentum is restricted to one half the Brillouin zone. Assuming a flux-free configuration,

$$h(\mathbf{k}) = \begin{pmatrix} 0 & J_x i & 0 & J_z i e^{-ik_1} & 0 & J_y i e^{-ik_4} \\ -J_x i & 0 & -J_y i & 0 & -J_z i e^{ik_2} & 0 \\ 0 & J_y i & 0 & J_x i & 0 & J_z i e^{-ik_3} \\ -J_z i e^{ik_1} & 0 & -J_x i & 0 & -J_y i & 0 \\ 0 & J_z i e^{-ik_2} & 0 & J_y i & 0 & J_x i \\ -J_y i e^{ik_4} & 0 & -J_z i e^{ik_2} & 0 & -J_x i & 0 \end{pmatrix}, \tag{11}$$

where the factor of 2 in the terms $2ic_ic_j$ in (7) has been absorbed into the antisymmetrization of the matrix. All momenta are resolved along the reciprocal lattice vectors, $\mathbf{k} = \sum_{a=1,4} k_a \boldsymbol{b_a}$, where $k_a = \mathbf{k}\cdot\boldsymbol{a_a}$. As in lower dimensions, the 4D Kitaev model has a sublattice symmetry linking odd and even sites. If we redefine the spinor to separate the odd and even sectors, $\tilde{c}^\dagger_{\mathbf{k}} = (c^\dagger_{1\mathbf{k}}, c^\dagger_{3\mathbf{k}}, c^\dagger_{5\mathbf{k}}, c^\dagger_{2\mathbf{k}}, c^\dagger_{4\mathbf{k}}, c^\dagger_{6\mathbf{k}})$, then $H = \sum_{\mathbf{k}\in\frac{1}{2}\text{BZ}} \tilde{c}^\dagger_{\mathbf{k}} \mathcal{H}(\mathbf{k}) \tilde{c}_{\mathbf{k}}$ acquires a compact, off-diagonal structure,

$$\mathcal{H}(\mathbf{k}) = \begin{pmatrix} & iQ(\mathbf{k}) \\ -iQ^\dagger(\mathbf{k}) & \end{pmatrix}, \quad Q(\mathbf{k}) = \begin{pmatrix} J_x & J_z e^{-ik_1} & J_y e^{-ik_4} \\ J_y & J_x & J_z e^{-ik_3} \\ J_z e^{-ik_2} & J_y & J_x \end{pmatrix}. \tag{12}$$

We note that the chiral operator $\Lambda = \sigma_z \otimes 1_3$ anticommutes with Λ, $\{\mathcal{H}(\mathbf{k}), \Lambda\} = 0$, guaranteeing that the spectrum is particle-hole symmetric. As in the Kitaev honeycomb model, the absence of next-nearest hopping terms is connected with the time-reversal symmetry of the underlying spin model. When we introduce Zeeman coupling terms, the equivalent Majorana representation develops next-nearest neighbor hopping which break this symmetry.

We now discuss the spectrum for the case of isotropic coupling constants ($J_x = J_y = J_z$) via the eigenvalue equation $\det[E - H(\mathbf{k})] = \det[E^2 - Q^\dagger(\mathbf{k})Q(\mathbf{k})] = 0$. Figure 4(a) shows the band structure along the closed path $\Gamma \to M \to X \to K \to L \to \Gamma$, where Γ is the origin while $M = \frac{1}{2}\boldsymbol{b_1}$, $X = \pi(\boldsymbol{b_1} - \boldsymbol{b_2})$, $K = \pi(\boldsymbol{b_1} - \boldsymbol{b_2} + \boldsymbol{b_3})$ and $L = \pi(\boldsymbol{b_1} - \boldsymbol{b_2} + \boldsymbol{b_3} + \boldsymbol{b_4})$. There is a fourfold degeneracy at the Γ, M, and L points which each connect a flat band to two linearly dispersing excitations. Along the high symmetry lines, the flat bands can be understood from the matrix structure of the Hamiltonian. For momenta located along the lines $\overrightarrow{\Gamma M}$ or $\overrightarrow{L\Gamma}$, the Q matrix is given by

$$\begin{aligned} Q(\mathbf{k}\in\overrightarrow{\Gamma M}) &= J\begin{pmatrix} 1 & e^{-is} & 1 \\ 1 & 1 & 1 \\ 1 & 1 & 1 \end{pmatrix}, \\ \mathbf{k} &= s\boldsymbol{b_1}, \quad 0 \leqslant s \leqslant \pi, \\ Q(\mathbf{k}\in\overrightarrow{\Gamma L}) &= J\begin{pmatrix} 1 & e^{it} & e^{it} \\ 1 & 1 & e^{it} \\ e^{-it} & 1 & 1 \end{pmatrix}, \\ \mathbf{k} &= -t(\boldsymbol{b_1} - \boldsymbol{b_2} + \boldsymbol{b_3} + \boldsymbol{b_4}), \quad 0 \leqslant t \leqslant \pi, \end{aligned} \tag{13}$$

and the corresponding determinants vanish along these lines. In fact, these flat bands are part of a two-dimensional Fermi surface, as we now discuss.

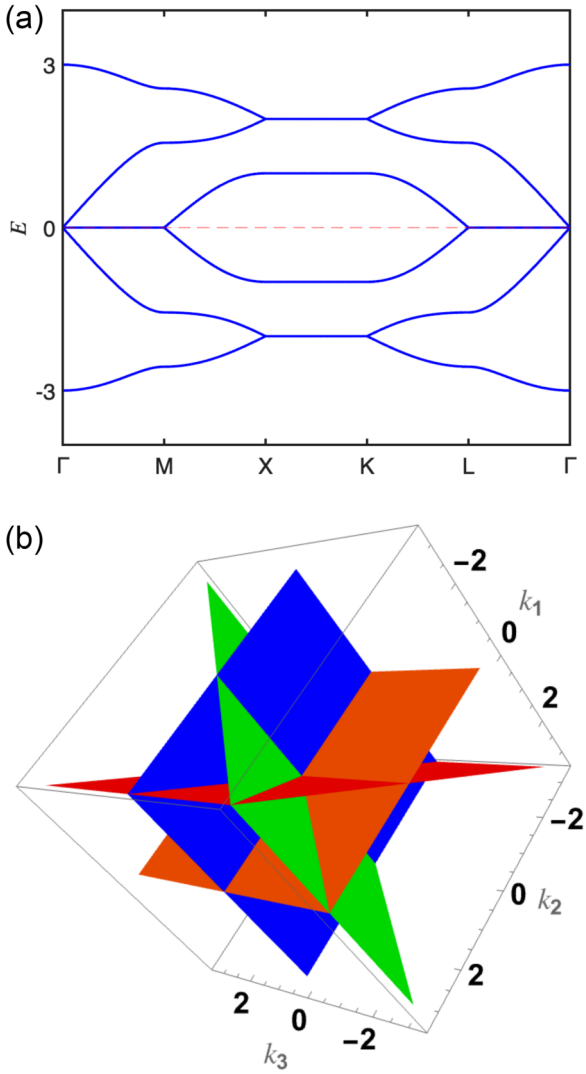


FIG. 4. (a) The spectrum along a high symmetry momentum path $\Gamma \to M \to X \to K \to L \to \Gamma$. (b) Four of the six two-dimensional Fermi surfaces defined in (14), projected into the first three dimensions (k_1, k_2, k_3).

B. Fermi surface

At the Fermi energy $E = 0$, the eigenvalue equation is $\det[Q] = 0$, which implies two independent constraints, $\mathrm{Re}[\det[Q]] = 0$ and $\mathrm{Im}[\det[Q]] = 0$, whose intersection defines a two-dimensional surface embedded within the four-dimensional Brillouin zone. As in lower dimensions, this surface of zero modes is protected via the an underlying projective symmetry [12,13] of the model. If we observe a slice of this Fermi surface projected into three dimensions at fixed $k_4 = t$, we obtain a string in three dimensions $\vec{k}(\theta, t)$, where θ defines the position along the string: as t varies, the string sweeps out a surface.

For the isotropic case, the Fermi surface can be identified by demanding that any two columns or rows of the matrix Q are proportional to one another. This gives rise to six separate surfaces of the following form :

$$(k_1, k_2, k_3, k_4) = \begin{cases} (t, s, 0, t), \\ (s, -t, t, t), \\ (0, s, t, t), \\ (t, -t, s, t), \\ (0, 0, s, t), \\ (s, 0, 0, t), \end{cases} \tag{14}$$

Figure 4(b) shows the first four of these Fermi surfaces projected into three dimensions.

C. Density of states

In the absence of the Van Hove singularity, a two-dimensional Fermi surface in a four-dimensional space leads to a density of states that is linear in energy $N(E) \propto E$. The eigenvalue equation is $\det[E^2 - Q(\mathbf{k})^\dagger Q(\mathbf{k})] = 0$. For a generic momentum on the Fermi surface where $E = 0$, $\det[Q(\boldsymbol{k_0})] = 0$, and the low-energy expansion in the vicinity of the Fermi surface at $\mathbf{k} = \mathbf{k}_0 + \delta\mathbf{k}$ is given by

$$E(\mathbf{k}) = \pm\sqrt{(\delta\mathbf{k} \cdot \nabla Q_1(\mathbf{k}_0))^2 + (\delta\mathbf{k} \cdot \nabla Q_2(\mathbf{k}_0))^2}, \tag{15}$$

where $Q(\mathbf{k}) = Q_1(\mathbf{k}) + iQ_2(\mathbf{k})$ separates the real and imaginary parts of the determinant. The density of states is then given by

$$D(E) = \int \frac{d^4k}{(2\pi)^4} \delta(|E| - \sqrt{(\delta\mathbf{k} \cdot \nabla Q_1)^2 + (\delta\mathbf{k} \cdot \nabla Q_2)^2}). \tag{16}$$

If we resolve the momenta into components parallel and perpendicular to the Fermi surface, writing $d^4k = d^2k_0 d^2k^\perp$, decomposing $\mathbf{k}^\perp = k_1^\perp \hat{\mathbf{e}}_1 + k_2^\perp \hat{\mathbf{e}}_2$, where $\hat{\mathbf{e}}_{1,2}$ are orthogonal normals to the Fermi surface, then we can write

$$\begin{aligned} D(E) &= \int \frac{d^2k_0}{(2\pi)^2} D(E, \mathbf{k}_0) \\ D(E, \mathbf{k}_0) &= \int \frac{d^2k^\perp}{(2\pi)^2} \delta(|E| - \sqrt{(\delta\mathbf{k} \cdot \nabla Q_1)^2 + (\delta\mathbf{k} \cdot \nabla Q_2)^2}). \end{aligned} \tag{17}$$

Changing variables to $u = \delta\mathbf{k} \cdot \nabla Q_1(\mathbf{k}_0)$ and $v = \delta\mathbf{k} \cdot \nabla Q_2(\mathbf{k}_0)$, then $d^2k^\perp = du dv / \det[\hat{e}^a \cdot \vec{\nabla} Q_b]$. Switching to polar coordinates $u + iv = re^{i\phi}$, then the energy $E(u, v) = r$, and the measure $du dv = 2\pi r dr$, so that

$$\begin{aligned} D(E, \mathbf{k}_0) &= \frac{1}{\det[\hat{e}^a \cdot \vec{\nabla} Q_b]} \int \frac{2\pi r dr}{(2\pi)^2} \delta(|E| - r) \\ &= \frac{|E|}{2\pi \det[\hat{e}^a \cdot \vec{\nabla} Q_b]} \end{aligned} \tag{18}$$

so that

$$D(E) = \frac{|E|}{2\pi} \int \frac{d^2k_0}{(2\pi)^2} \frac{1}{\det[\hat{e}^a \cdot \vec{\nabla} Q_b]}, \tag{19}$$

demonstrating that the density of states $D(E)$ depends linearly on energy. As a comparison with the analytical

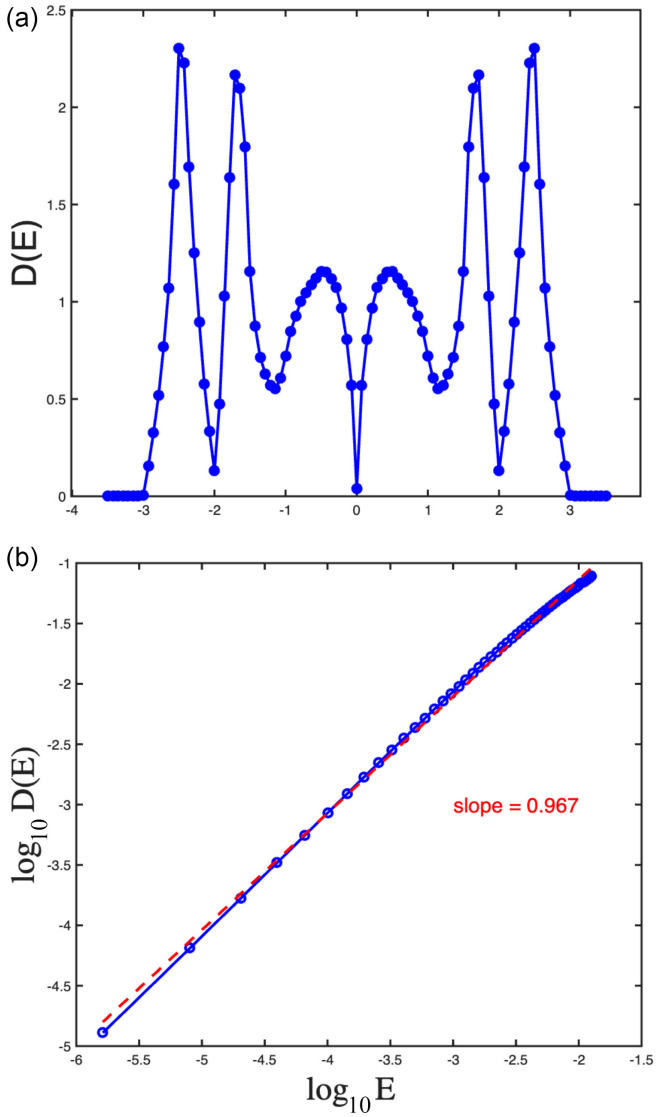


FIG. 5. (a) The density of state as a function of energy. At zero energy, the density of states is zero, suggesting that the dimension of the Fermi surface is lower than three. (b) Semilog plot for the DOS versus energy, with a slope that is consistent with $D(E) \propto |E|$.

result, we have computed the density of the states $D(E) = \frac{1}{\pi N}\sum_k \mathrm{Im}[Tr(G_0(E - i0^+, \mathbf{k}))]$ numerically as shown in Fig. 5(a). A fit to the low energy density of states [see Fig. 5(b)] confirms $D(E) \propto |E|$.

D. The ground state

As in the 2D case, the ground state excitations of the 4D Kitaev model maps onto a problem of free fermions, with diagonalized Hamiltonian

$$H = \sum_{\mathbf{k}\in\frac{1}{2}\mathrm{BZ},n\in[1,6]} E_{\mathbf{k}n} d^\dagger_{\mathbf{k}n} d_{\mathbf{k}n}, \tag{20}$$

where $d^\dagger_{\mathbf{k},m}$ is the quasiparticle creation operator, $E_{\mathbf{k}n}$ are the corresponding eigenstates and the sum runs over one-half of the Brillouin zone. We assume that the eigenstates are ordered, such that $E_{\mathbf{k}n} < 0$ for $n \in [1, 3]$. The ground state is then given

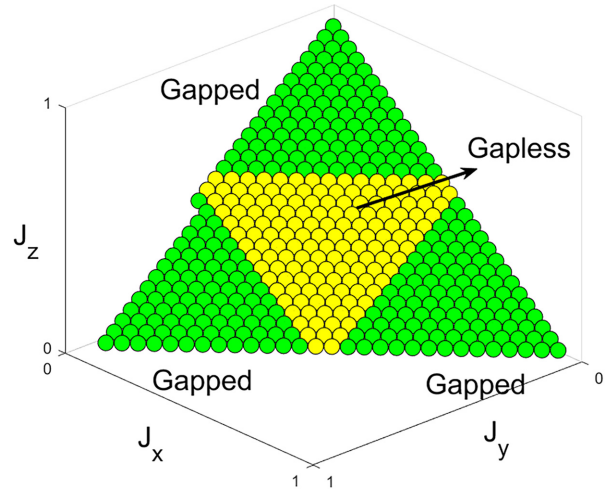


FIG. 6. Gapped-gapless phase diagram as a function of J_x, J_y, J_z. The diagram looks very similar to the one for the 2D honeycomb model.

by the filled Fermi sea

$$|GS\rangle = \prod_{\mathbf{k}\in\frac{1}{2}\mathrm{BZ},n\in[1,3]} d^\dagger_{\mathbf{k}n}|0\rangle, \tag{21}$$

where the product over band-index is restricted to the first three negative energy quasiparticle states. The corresponding ground state energy is the summation of all negative energies

$$E_G = \frac{1}{2}\sum_{n=1-3}\int \frac{d^4k}{(2\pi)^4} E_{\mathbf{k}n}. \tag{22}$$

Evaluating the ground state energy numerically, we obtain $E_G = -2.29J$.

E. The anisotropic coupling constants

We also identify the phase transition between the gapless phase and the gapped phase by tuning the anisotropy between the three coupling constants J_x, J_y, J_z (see Fig. 6). In contrast to the two-dimensional honeycomb lattice, where the equation for the gapless condition can be handled analytically, the parameter region that corresponds to gapped phases in our 4D model can only be numerically determined. To map out the phase diagram, we compute the minimum value of the gap between the eigenvalues $\Delta_g = \min(E_4(\mathbf{k}) - E_3(\mathbf{k}))$ delineating the regions where $\Delta_g > 0$ is finite.

From the phase diagram, it is obvious that if the three coupling constants largely deviate from each other, the system is gapped, much similar to the case in the Kitaev honeycomb model [6]. This result also suggests the possibility of realizing the topological order and non-Abelian anyon in our model.

IV. VISON GAP

Although the energy spectrum and energy of the flux-free state are obtained in the previous section, one should notice that all the theoretical calculation done so far is based on the flux-free assumption. Central to our work is the assumption that the zero-flux state is energetically favorable. Although

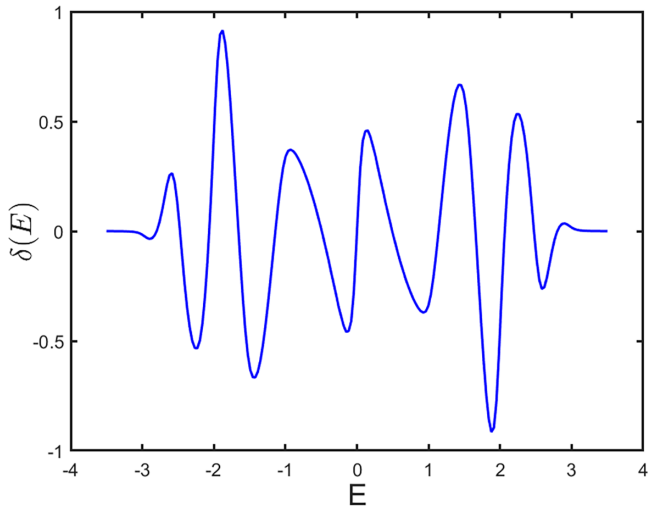


FIG. 7. Energy dependence of the scattering phase shift resulting from bond flipping in the hyperhexagonal Kitaev model. The energy is expressed in the unit of J.

the Lieb theorem states that the ground state is flux-free for a two-dimensional system, the theorem only applies to two dimensions. To confirm that the vortex-free configuration is the lowest energy state in our model, we need to confirm that the energy of single bond flip is positive, allowing stability against gauge fluctuations.

To carry out this calculation, we follow the methodology of [37], evaluating the energy cost of a bond flip in terms of the Majorana scattering phase shift. For simplicity, we consider the isotropic case ($J_x = J_y = J_z = J$). The formalism is summarized in the Appendix B. Here we only mention the crucial results. The presence of the bond flipping potential causes the phase shift and the energy change due to the vison creation is given by the energy integration of the phase shift $\Delta F = \int_0^\infty dE \frac{\delta(E)}{2\pi}$, where $\delta(E)$ is the scattering phase shift. Figure 7 shows our numerical calculation of the $\delta(E)$ in the case where the bond variable between third and fourth atoms $u_{\langle 34\rangle}$ is flipped. After numerical integration, we find that the change of energy due to the bond flip is positive, given by $0.0234(J)$. This numerical calculation confirms that the flux-free state is locally stable against gauge fluctuations.

V. DISCUSSION AND CONCLUSION

Here we discuss some of the forward implications of our work and some of the open questions it poses.

A. Fractionalization and the Yao-Lee extension

The factorization of the spin operator

$$\vec{\sigma}_j = 2ia_j\vec{b}_j \tag{23}$$

into a bilinear of free fermions, together with the positive vison energy computed in Sec. IV is a strong indicator of fractionalization in our 4D Kitaev spin liquid. As in lower dimensional spin liquids, a spin-flip creates a mobile Majorana while also creating two visons, thus a strict statement about the fractionalization requires some knowledge of the statistical mechanics of the static Z_2 gauge fields. For example, confirmation that the spin susceptibilty involves a continuum of excitations above the vison gap requires a study of the vison correlation functions, which requires numerical methods [38]. In two dimensions, the separation of Majorana and gauge degrees of freedom can also be confirmed by showing that the specific heat curves separate into a low-temperature Majorana component and a high temperature gauge component, each carrying entropy $\frac{1}{2}\ln 2$ per site [39].

However, in three and higher dimensions, fractionalization is guaranteed by the properties of the Z_2 gauge fields. When the fermions are integrated out of the partition function, the remaining effective action describes a pure Z_2 lattice gauge theory, which is subject to a finite temperature Ising transition between a high temperature area-law phase and a low temperature perimeter law phase in which the visons are confined [40,41]. The presence of this transition in ($D > 2$) Kitaev models has been explicitly confirmed without performing a heavy numerical calculation. Below the Ising transition temperature, the Majorana fermion a_j becomes a free fermion, guaranteeing a fractionalized phase.

An even clearer rendition of this fractionalization can be obtained by constructing the corresponding Yao-Lee model on the hyperhexagonal lattice. Here we can identify the formation of a Yao-Lee spin liquid (YLSL) with gapless, fractionalized spin excitations [18,42]. The Yao-Lee generalization of a Kitaev model incorporates an additional spin-1/2 orbital degree of freedom λ_j^α ($\alpha = 1-3$), in addition to a spin degree of freedom $\vec{\sigma}_j$ at each site, where the $\vec{\lambda}_j$ and $\vec{\sigma}_j$ are independent Pauli matrices. The Yao-Lee Hamiltonian

$$H = J\sum_{\langle i,j\rangle} \lambda_i^{\alpha_i}\lambda_j^{\alpha_j}(\vec{\sigma}_i\cdot\vec{\sigma}_j) \tag{24}$$

involves a frustrated Ising coupling between the orbital fields, decorated by a Heisenberg interaction between the spin fields. In this model, the factorization of Pauli operators involves defining a triplet of Majorana fermions $\vec{b}_j = (b_j^1, b_j^2, b_j^3)$ and $\vec{\chi}_j = (\chi_j^1, \chi_j^2, \chi_j^3)$ [18]. Within this representation, the Pauli operators can be written as

$$\begin{aligned}\vec{\sigma}_j &= -i\vec{\chi}_j\times\vec{\chi}_j,\\ \vec{\lambda}_j &= -i\vec{b}_j\times\vec{b}_j.\end{aligned} \tag{25}$$

After the substitution, the Hamiltonian can be expressed as

$$H = J\sum_{\langle i,j\rangle}\hat{u}_{ij}(i\vec{\chi}_i\cdot\vec{\chi}_j), \tag{26}$$

where $\hat{u}_{ij} = -2ib_i^{\alpha_i}b_j^{\alpha_j}$. One can observe that the gauge degree of freedom is carried solely by the orbital Majorana fermions $\vec{b}_j$ and is decoupled from spin components. Therefore, a spin-flip no longer involves the gauge field and the creation of visons. Thus in the Yao-Lee extension of our model, we can ensure that the spin fractionalizes into gapless particles, and that the dynamical spin susceptibility acquires a gapless Lindhard continuum associated with the 2D Majorana Fermi surface.

B. Jordan-Wigner transformation

We can also derive the same results using the Jordan-Wigner transformation [43]. This approach can be applied to the Kitaev model and its variants, as discussed in Refs. [44–46]. The string operator, which enforces the commutivity of spins at different sites, is an essential element of the Jordan-Wigner transformation and can be consistently defined with open boundary conditions. Usually, a Jordan-Wigner transformation in higher-dimensional models gives rise to long nonlocal strings. Fortunately, a Kitaev-type model eliminates this issue, since the bonds separating the strings are z bonds, which create interchain gauge fields that do not interfere with the locality of the model. The construction of the string operator relies on the definition of an ordered path using open boundary conditions. The path to a given site j advances along each spiral chain, sweeping in a fixed sequence between spirals across all dimensions transverse to the chains until it arrives at site j. The Jordan-Wigner transform at site j is

$$\begin{aligned} S_j^+ &= c_j^\dagger P_j \\ S_j^- &= c_j P_j \\ S_i^z &= c_j^\dagger c_j - 1, \end{aligned} \tag{27}$$

where c_j denotes a spinless fermion operator at site j, $P_j = e^{i\Phi_j}$, where $\Phi_j = \pi \sum_{l<j} n_l$ is the string operator along to the ordered path ending at site j. Dividing the lattice into two sub-lattices labeled by even and odd-numbered sites, we then decompose the complex fermions into their Majorana components [18,45], writing $c_j = (\chi_{A,j} + i\chi_{B,j})/\sqrt{2}$ ($j \in$ even number) and $c_j = (\chi_{A,j} - i\chi_{B,j})/\sqrt{2}$ ($j \in$ odd number), the Hamiltonian then takes the form

$$\begin{aligned} H = J_x \sum_{\substack{i\in\text{even} \\ \langle ij\rangle\in\text{x-bond}}} (i\chi_{A,i}\chi_{A,j}) + J_y \sum_{\substack{i\in\text{even} \\ \langle ij\rangle\in\text{y-bond}}} (i\chi_{A,i}\chi_{A,j}) \\ + J_z \sum_{\substack{i\in\text{even} \\ \langle ij\rangle\in\text{z-bond}}} D_{ij}(i\chi_{A,i}\chi_{A,j}), \end{aligned} \tag{28}$$

The B Majoranas only appear in the bond variables $D_{ij} = -2i\chi_{B,i}\chi_{B,j}$, which have eigenvalues ± 1. Since each D_{ij} lives on a z bond and does not overlap with each other, this operator commutes with the Hamiltonian and becomes a constant of motion. This then reverts to Hamiltonian (7), but in the gauge where the u_{ij} are restricted to lie along the z bonds between the chains. In this way, we see that the Jordan-Wigner transformation works in four dimensions.

C. Finite Zeeman field

In addition, based on our 4D model, one can ask how the system behaves in the presence of a magnetic field. In the Kitaev honeycomb model [6], a magnetic Zeeman coupling induces a next-nearest neighboring hopping term which leads to a topological gap opening and formation of a Chern insulator, in analogy to the Haldane model [47]. In principle, four dimension systems allow for the existence of non-Abelian Chern insulators characterized by the second Chern number C_2, provided the field continues to induce a gap. In the presence of a Zeeman coupling $-\mathbf{h}\cdot\sigma_{\mathbf{j}}$ at each site, the Majorana Hamiltonian develops next-nearest neighbor hopping terms, giving rise to a Hamiltonian of the form $H = \sum_{\mathbf{k}} \tilde{c}_{\mathbf{k}}^\dagger [\mathcal{H}(\mathbf{k}) + \Lambda(\mathbf{k})]\tilde{c}_{\mathbf{k}}$ where $\mathcal{H}(\mathbf{k})$ is given in (12) and

$$\Lambda(\mathbf{k}) = \begin{pmatrix} F(\mathbf{k}) & 0 \\ 0 & -G(\mathbf{k}) \end{pmatrix} \tag{29}$$

has a block-diagonal structure with

$$F(\mathbf{k}) = -\alpha \frac{h_x h_y h_z}{J^2} \begin{pmatrix} 0 & -if_{13} & if_{15} \\ if_{13}^* & 0 & -if_{35} \\ -if_{15}^* & if_{35}^* & 0 \end{pmatrix} \tag{30}$$

and

$$G(\mathbf{k}) = -\alpha \frac{h_x h_y h_z}{J^2} \begin{pmatrix} 0 & -if_{24} & if_{26} \\ if_{24}^* & 0 & -if_{46} \\ -if_{26}^* & if_{46}^* & 0 \end{pmatrix}, \tag{31}$$

where $\alpha \sim O(1)$ is a number of order unity, h_x, h_y, h_z are the components of the applied field and

$$\begin{aligned} f_{13} &= 1 + e^{-ik_1} + e^{i(k_3-k_4)}, \\ f_{15} &= e^{-ik_1} + e^{ik_2} + e^{-ik_4}, \\ f_{35} &= 1 + e^{ik_2} + e^{-ik_3}, \end{aligned} \tag{32}$$

and

$$\begin{aligned} f_{24} &= 1 + e^{-ik_1} + e^{ik_2}, \\ f_{26} &= e^{ik_2} + e^{-ik_3} + e^{-ik_4}, \\ f_{46} &= 1 + e^{i(k_1-k_4)} + e^{-ik_3} \end{aligned} \tag{33}$$

are the form factors for next-nearest neighbor hopping.

In a 2D Kitaev model, $\mathcal{H}(\mathbf{k}) + \Lambda(\mathbf{k}) = \vec{d}(\mathbf{k})\cdot\vec{\sigma}$ can be decomposed in a set of anticommuting Pauli matrices, giving rise to a dispersion $E_{\mathbf{k}} = \pm|\vec{d}(\mathbf{k})|$. When there are only two components to $\vec{d}(\mathbf{k})$, the condition that $E(\mathbf{k}) = 0$ defines two constraints, defining the two gapless Dirac points, but in a magnetic field, the condition that three components vanish cannot be satisfied anywhere in momentum space, leading to a gapped spectrum. By contrast, in the 4D Kitaev model, $\{\mathcal{H}(\mathbf{k}), \Lambda(\mathbf{k})\} \neq 0$ and the complex-valued condition $\det Q(\mathbf{k}) = Q_1(\mathbf{k}) + iQ_2(\mathbf{k}) = 0$ which defines a 2D Fermi surface with a vanishing density of states in zero field becomes a single, real-valued condition $\det[\mathcal{H}(\mathbf{k}) + \Lambda(\mathbf{k})] = 0$ in a field. This condition now defines a 3D Fermi surface. In this situation, the spin liquid in a Zeeman field develops a *finite* density of states. Numerical calculations shown in Fig. 8 confirm this expectation, showing the development of a finite density of states proportional to $h_x h_y h_z$. This rules out the formation of a topological gapped state in our model.

D. Conclusion

To conclude, we have proposed an exactly solvable four-dimensional Kitaev model. The key ingredient is a spiral structure which allows a well-defined Jordan-Wigner string. Our model calculation demonstrates that the 4D Kitaev spin model possesses a two-dimensional Majorana Fermi surface. We have used scattering theory to compute the energy cost to create a vison, demonstrating that the state with zero-flux is locally stable. Furthermore, we also examine the effect of the

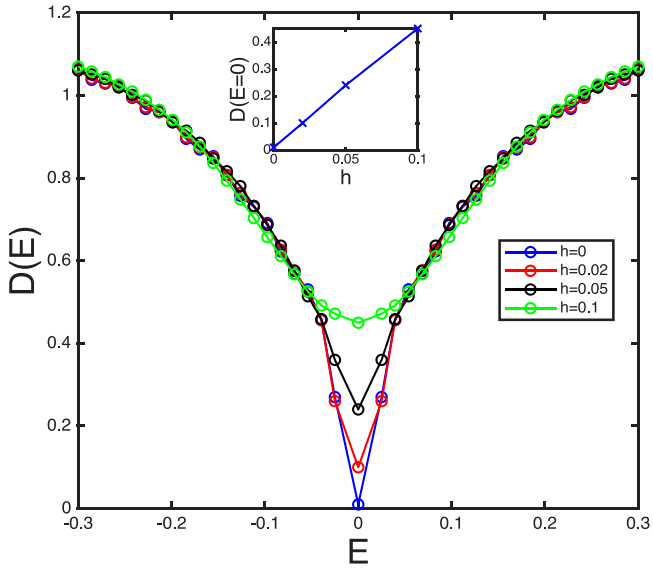


FIG. 8. Density of state as a function of energy. The three curves correspond to three different field strengths $h = \frac{h_x h_y h_z}{J^2} = 0, 0.02, 0.05, 0.1$. The inset plot shows the density of state at Fermi energy $E = 0$ as a function of field strength.

Zeeman field. Contrary to expectations, our model develops a three-dimensional Fermi surface in a field, with a finite density of states proportional to the cube of the applied fields. Our 4D model opens a new venue for exploring high dimensional topological phases and inspires several open questions. For instance, one can ask whether our model can be extended to higher dimensions. Clearly the spiral motif can be extended to higher dimensions, but without further work, it is not yet clear that the resulting structures will close to produce a consistent crystal structure.

Another challenge for future work is to further explore whether a fully gapped non-Abelian phase can be found in a four-dimensional generalization of a Kitaev model. For this purpose, it might be useful to employ a higher-dimensional Clifford algebra which allows lattices with larger coordination numbers, as discussed in Ref. [48].

ACKNOWLEDGMENTS

We would like to thank Aaditya Panigrahi for fruitful discussions. This work was supported by Office of Basic Energy Sciences, Material Sciences and Engineering Division, U.S. Department of Energy (DOE) under Contract No. DE-FG02-99ER45790.

DATA AVAILABILITY

The data that support the findings of this article are openly available [49].

APPENDIX A: THE HYPERHEXAGONAL LATTICE

Here, we provide a detailed description of the hyperhexagonal lattice. All vectors used in the following calculation are depicted in Fig. 9. Recall the vectors connecting different sites

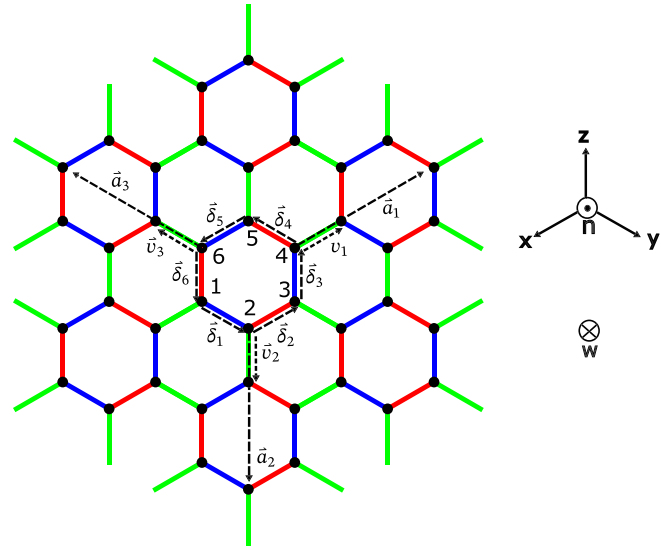


FIG. 9. The projected 2D lattice structure of the hyperhexagonal lattice. The projection direction is $\hat{n} = (1, 1, 1, 0)$. The blue-red bonds denote xx, yy alternative bonds, while the green bonds represent zz bonds.

inside a unit cell,

$$\begin{aligned} \boldsymbol{\delta_1} &= (0, 1, 0, 1), \\ \boldsymbol{\delta_2} &= (-1, 0, 0, 0), \\ \boldsymbol{\delta_3} &= (0, 0, 1, 1), \\ \boldsymbol{\delta_4} &= (0, -1, 0, 0), \\ \boldsymbol{\delta_5} &= (1, 0, 0, 1), \\ \boldsymbol{\delta_6} &= (0, 0, -1, 0), \end{aligned} \tag{A1}$$

where only $\boldsymbol{\delta_1}, \boldsymbol{\delta_3}$, and $\boldsymbol{\delta_5}$ have a nonvanishing fourth component. We also define the linking vectors $\boldsymbol{v_1}, \boldsymbol{v_2}$, and $\boldsymbol{v_3}$ connecting the neighboring unit cells.

$$\begin{aligned} \boldsymbol{v_1} &= \tfrac{1}{2}(-1, 1, 1, 0), \\ \boldsymbol{v_2} &= \tfrac{1}{2}(1, 1, -1, 0), \\ \boldsymbol{v_3} &= \tfrac{1}{2}(1, -1, 1, 0). \end{aligned} \tag{A2}$$

Our choice of vector follows the rule that the lengths of vectors $\boldsymbol{v_i}$ are the same as those of red and blue bonds. This setup allows us to define three Bravais lattice vectors characterizing the periodicity of the lattice geometry,

$$\begin{aligned} \boldsymbol{a}_1 &= \boldsymbol{\delta}_1 + \boldsymbol{\delta}_2 + \boldsymbol{\delta}_3 + \boldsymbol{v}_1 = \left(-\tfrac{3}{2}, \tfrac{3}{2}, \tfrac{3}{2}, 2\right) \\ \boldsymbol{a}_2 &= \boldsymbol{\delta}_2 + \boldsymbol{\delta}_3 + \boldsymbol{\delta}_4 + \boldsymbol{v}_2 = \left(\tfrac{3}{2}, \tfrac{3}{2}, -\tfrac{3}{2}, -1\right) \\ \boldsymbol{a}_3 &= \boldsymbol{\delta}_3 + \boldsymbol{\delta}_4 + \boldsymbol{\delta}_5 + \boldsymbol{v}_3 = \left(\tfrac{3}{2}, -\tfrac{3}{2}, \tfrac{3}{2}, 2\right) \\ \boldsymbol{a}_4 &= \boldsymbol{\delta}_1 + \boldsymbol{\delta}_2 + \boldsymbol{\delta}_3 + \boldsymbol{\delta}_4 + \boldsymbol{\delta}_5 + \boldsymbol{\delta}_6 = (0, 0, 0, 3). \end{aligned} \tag{A3}$$

Next, we will show that the lattice geometry in a two-dimensional projected space is identical to the honeycomb lattice structure. To begin with, we aim to obtain vectors that describe the lattice geometry in a two-dimensional projected space. To do this, we first project out the fourth component [the projection direction is $\boldsymbol{w} = (0, 0, 0, 1)$]. The second step is to project out a particular direction in the 3D space. Thus,

we introduce the normal vector $\boldsymbol{n} = \frac{1}{\sqrt{3}}(1, 1, 1, 0)$. We then define an operator for the two-step projection,

$$P = I_{4\times4} - \boldsymbol{n}\boldsymbol{n}^T - \boldsymbol{w}^T\boldsymbol{w} = \frac{1}{3}\begin{pmatrix} 2 & -1 & -1 & 0 \\ -1 & 2 & -1 & 0 \\ -1 & -1 & 2 & 0 \\ 0 & 0 & 0 & 0 \end{pmatrix}. \tag{A4}$$

The projected vectors are then

$$\begin{aligned}
\boldsymbol{\delta}_{1,2D} &= P\boldsymbol{\delta}_1 = \left(-\tfrac{1}{3}, \tfrac{2}{3}, -\tfrac{1}{3}, 0\right)^T \\
\boldsymbol{\delta}_{2,2D} &= P\boldsymbol{\delta}_2 = \left(-\tfrac{2}{3}, \tfrac{1}{3}, \tfrac{1}{3}, 0\right)^T \\
\boldsymbol{\delta}_{3,2D} &= P\boldsymbol{\delta}_3 = \left(\tfrac{-1}{3}, \tfrac{-1}{3}, \tfrac{2}{3}, 0\right)^T \\
\boldsymbol{\delta}_{4,2D} &= P\boldsymbol{\delta}_4 = \left(\tfrac{1}{3}, -\tfrac{2}{3}, \tfrac{1}{3}, 0\right)^T \\
\boldsymbol{\delta}_{5,2D} &= P\boldsymbol{\delta}_5 = \left(\tfrac{2}{3}, -\tfrac{1}{3}, -\tfrac{1}{3}, 0\right)^T \\
\boldsymbol{\delta}_{6,2D} &= P\boldsymbol{\delta}_6 = \left(\tfrac{1}{3}, \tfrac{1}{3}, -\tfrac{2}{3}, 0\right)^T \\
\boldsymbol{v}_{1,2D} &= P\boldsymbol{v}_1 = \left(-\tfrac{2}{3}, \tfrac{1}{3}, \tfrac{1}{3}, 0\right)^T \\
\boldsymbol{v}_{2,2D} &= P\boldsymbol{v}_2 = \left(\tfrac{1}{3}, \tfrac{1}{3}, -\tfrac{2}{3}, 0\right)^T \\
\boldsymbol{v}_{3,2D} &= P\boldsymbol{v}_3 = \left(\tfrac{1}{3}, -\tfrac{2}{3}, \tfrac{1}{3}, 0\right)^T
\end{aligned} \tag{A5}$$

Since we have projected out two degrees of freedom, we can define two basis vectors $\hat{\boldsymbol{x}} = \frac{1}{\sqrt{2}}(-1, 1, 0, 0)$ and $\hat{\boldsymbol{y}} = \frac{1}{\sqrt{6}}(-1, -1, 2, 0)$ to reexpress the above vectors. A simple algebra leads to the following results:

$$\begin{aligned}
\boldsymbol{\delta}_{1,2D} &= \frac{1}{\sqrt{2}}\hat{\boldsymbol{x}} - \frac{1}{\sqrt{6}}\hat{\boldsymbol{y}}, \quad \boldsymbol{\delta}_{2,2D} = \frac{1}{\sqrt{2}}\hat{\boldsymbol{x}} + \frac{1}{\sqrt{6}}\hat{\boldsymbol{y}} \\
\boldsymbol{\delta}_{3,2D} &= \sqrt{\frac{2}{3}}\hat{\boldsymbol{y}}, \quad \boldsymbol{\delta}_{4,2D} = -\frac{1}{\sqrt{2}}\hat{\boldsymbol{x}} + \frac{1}{\sqrt{6}}\hat{\boldsymbol{y}}, \\
\boldsymbol{\delta}_{5,2D} &= -\frac{1}{\sqrt{2}}\hat{\boldsymbol{x}} - \frac{1}{\sqrt{6}}\hat{\boldsymbol{y}}, \quad \boldsymbol{\delta}_{6,2D} = -\sqrt{\frac{2}{3}}\hat{\boldsymbol{y}} \\
\boldsymbol{v}_{1,2D} &= \frac{1}{\sqrt{2}}\hat{\boldsymbol{x}} + \frac{1}{\sqrt{6}}\hat{\boldsymbol{y}} \\
\boldsymbol{v}_{2,2D} &= -\sqrt{\frac{2}{3}}\hat{\boldsymbol{y}} \\
\boldsymbol{v}_{3,2D} &= -\frac{1}{\sqrt{2}}\hat{\boldsymbol{x}} + \frac{1}{\sqrt{6}}\hat{\boldsymbol{y}}
\end{aligned} \tag{A6}$$

It is easy to prove that all these vectors can form a hexagonal structure in a 2D space as shown in Fig. 9.

APPENDIX B: SCATTERING THEORY

As mentioned in the main text, the flux-free state is not necessarily the ground state in our model since the validity of Lieb theorem [50] is not guaranteed in a higher-dimensional system. To examine whether the flux-free state is the ground state, we consider a scenario where the visons are created via flipping a gauge-embedded bond. We then adapt the scattering theoretic description, treating the bond flip as a scattering potential. Subsequently, we utilize the Green's function approach [19,37] to evaluate the change of free energy due to flipping a bond on the lattice. Let us consider the case of flipping a single bond u_{ij} for a xx or a yy bond. We then rewrite the Hamiltonian as a flux-free part and bond-flip part, $H = H_0 + V$, where

$$\begin{aligned}
H_0 &= \sum_{i,j} 2iJ_{\alpha_{ij}} u_{\langle ij\rangle} c_i c_j, \quad \text{with all } u_{\langle ij\rangle} = 1, \\
V &= -4J_{\alpha_{ab}} i c_a c_b.
\end{aligned} \tag{B1}$$

Here, the index a, b denote two adjacent atoms within the unit cell. To calculate the vison gap, we first write down the free energy as

$$F = \frac{-1}{2\beta}\sum_{\omega,k} \mathrm{tr}(\ln(-G^{-1})), \tag{B2}$$

where $\beta = 1/T$. The factor $\frac{1}{2}$ on the right-hand side prevents the double counting of modes in the Brillouin zone. The trace denotes the summation over the sublattice degree of freedom. G is the Green's function, which can be expressed as $G = (G_0^{-1} - V)^{-1}$. G_0 is a flux-free Green's function given by

$$G_0(i\omega, \mathbf{k}) = \frac{1}{i\omega - H_0(\mathbf{k})} = \sum_n \frac{|\psi_n\rangle\langle\psi_n|}{i\omega - \epsilon_n(\mathbf{k})}. \tag{B3}$$

$\epsilon_n(k)$ represents the eigenenergy of the Hamiltonian $H_0(k)$ and $|\Psi_n\rangle$ is the corresponding eigenstate. Separating zero-flux free energy and change of free energy due to scattering potential, it yields

$$\Delta F = -\frac{-1}{2\beta}\sum_{i\omega_n} \mathrm{tr}\left(1 - \hat{V}\sum_k G_0(i\omega, \mathbf{k})\right). \tag{B4}$$

For our convenience, one can define the local Green's function

$$g(i\omega_n) = \sum_k G_0(i\omega_n, \mathbf{k}). \tag{B5}$$

Thus, the change of free energy becomes

$$\Delta F = \frac{-1}{2\beta}\sum_{i\omega} \mathrm{tr}(1 - \hat{V}g(i\omega_n)). \tag{B6}$$

Additionally, the bond-flipping potential can be expressed in matrix form

$$\hat{V} = VO_m \oplus \sigma_2 \oplus O_{4-m}, \tag{B7}$$

where V is the coupling constant and σ_2 is the Pauli-y matrix. O_m is a m by m null matrix, and the index m denotes bond flipping between $m + 1^{th}$ and $m + 2^{th}$ atoms. As noted in the main text, we consider the case where bond flipping occurs at the bond connecting third and fourth atoms,or equivalently, $m = 2$. Therefore, the final expression of the free energy is

$$\Delta F = \frac{-1}{2\beta}\sum_{i\omega_n} \mathrm{tr}(\ln(1 - VO_2 \oplus \sigma_2 \oplus O_2 g(i\omega_n))). \tag{B8}$$

The trace of the logarithm function can be further simplified as the logarithm of the determinant of the matrix. It yields

$$\Delta F = \frac{-1}{2\beta}\sum_{i\omega_n,\alpha} \ln\lambda_\alpha(i\omega_n), \tag{B9}$$

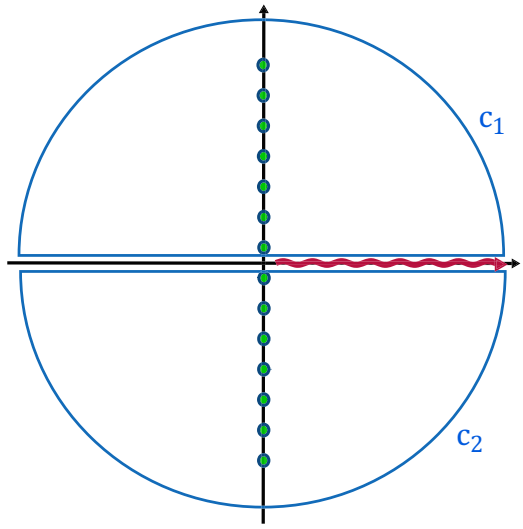


FIG. 10. The contour C_1, C_2 for a known branch cut.

where λ_α is an eigenvalue of $1 - \hat{V}O_2 \oplus \sigma_2 \oplus O_2 g(i\omega_n)$. We can further evaluate the Matsubara summation by converting the summation into a real energy integral, see Fig. 10.

$$\Delta F = -\int_{-\infty}^{\infty} \frac{d\omega}{2\pi} f(\omega) \mathrm{Im} \ln \lambda_\alpha(\omega)$$
$$= -\int_{-\infty}^{\infty} \frac{d\omega}{2\pi} f(\omega)\delta(\omega). \tag{B10}$$

Here, $\delta(\omega)$ denotes the scattering phase shift. Since the phase shift is odd in frequency ($\delta(-\omega) = -\delta(\omega)$). At zero temperature, the integral can be reexpressed,

$$\Delta F = \int_{0}^{\infty} \frac{d\omega}{2\pi} \delta(\omega). \tag{B11}$$

The remaining part of the calculation is performed numerically. Performing the numerical integration, one can obtain that the single bond flip energy is around 0.0234(J). The energy cost to create visons is positive, indicating that the flux-free state has the lowest energy among all possible gauge configurations. Another issue is the energy cost to flip a zz bond. The scattering potential would be nonlocal since the two points forming zz bonds belong to different unit cells, according to our definition. A straightforward symmetry argument tells us the energy cost to flip a zz bond is different from that of flipping xx, yy bonds.

[1] P. W. Anderson, The resonating valence bond state in La_2CuO_4 and superconductivity, Science **235**, 1196 (1987).

[2] P. Anderson, Resonating valence bonds: A new kind of insulator? Mater. Res. Bull. **8**, 153 (1973).

[3] L. Savary and L. Balents, Quantum spin liquids: a review, Rep. Prog. Phys. **80**, 016502 (2017).

[4] L. Balents, Spin liquids in frustrated magnets, Nature (London) **464**, 199 (2010).

[5] J. Wen, S.-L. Yu, S. Li, W. Yu, and J.-X. Li, Experimental identification of quantum spin liquids, npj Quantum Mater. **4**, 12 (2019).

[6] A. Kitaev, Anyons in an exactly solved model and beyond, Ann. Phys. **321**, 2 (2006).

[7] V. Lahtinen and J. K. Pachos, A short introduction to topological quantum computation, SciPost Phys. **3**, 021 (2017).

[8] C. Nayak, S. H. Simon, A. Stern, M. Freedman, and S. Das Sarma, Non-Abelian anyons and topological quantum computation, Rev. Mod. Phys. **80**, 1083 (2008).

[9] S. Mandal and N. Surendran, Exactly solvable Kitaev model in three dimensions, Phys. Rev. B **79**, 024426 (2009).

[10] M. Hermanns and S. Trebst, Quantum spin liquid with a Majorana Fermi surface on the three-dimensional hyperoctagon lattice, Phys. Rev. B **89**, 235102 (2014).

[11] M. Hermanns, K. O'Brien, and S. Trebst, Weyl spin liquids, Phys. Rev. Lett. **114**, 157202 (2015).

[12] K. O'Brien, M. Hermanns, and S. Trebst, Classification of gapless $\mathbb{Z}_2$ spin liquids in three-dimensional Kitaev models, Phys. Rev. B **93**, 085101 (2016).

[13] M. G. Yamada, V. Dwivedi, and M. Hermanns, Crystalline Kitaev spin liquids, Phys. Rev. B **96**, 155107 (2017).

[14] T. Eschmann, P. A. Mishchenko, K. O'Brien, T. A. Bojesen, Y. Kato, M. Hermanns, Y. Motome, and S. Trebst, Thermodynamic classification of three-dimensional Kitaev spin liquids, Phys. Rev. B **102**, 075125 (2020).

[15] S. S. Jahromi, H. Yarloo, and R. Orús, Thermodynamics of three-dimensional Kitaev quantum spin liquids via tensor networks, Phys. Rev. Res. **3**, 033205 (2021).

[16] M. G. Yamada, Topological Z_2 invariant in Kitaev spin liquids: Classification of gapped spin liquids beyond projective symmetry group, Phys. Rev. Res. **3**, L012001 (2021).

[17] P. Coleman, A. Panigrahi, and A. Tsvelik, Solvable 3D Kondo lattice exhibiting pair density wave, odd-frequency pairing, and order fractionalization, Phys. Rev. Lett. **129**, 177601 (2022).

[18] A. M. Tsvelik and P. Coleman, Order fractionalization in a Kitaev-Kondo model, Phys. Rev. B **106**, 125144 (2022).

[19] A. Panigrahi, A. Tsvelik, and P. Coleman, Breakdown of order fractionalization in the CPT model, Phys. Rev. B **110**, 104520 (2024).

[20] S.-H. Do, S.-Y. Park, J. Yoshitake, J. Nasu, Y. Motome, Y. Kwon, D. T. Adroja, D. J. Voneshen, K. Kim, T.-H. Jang, J.-H. Park, K.-Y. Choi, and S. Ji, Majorana fermions in the Kitaev quantum spin system α-$RuCl_3$, Nat. Phys. **13**, 1079 (2017).

[21] K. Mehlawat, A. Thamizhavel, and Y. Singh, Heat capacity evidence for proximity to the Kitaev quantum spin liquid in A_2IrO_3 (A = Na, Li), Phys. Rev. B **95**, 144406 (2017).

[22] S. M. Winter, A. A. Tsirlin, M. Daghofer, J. van den Brink, Y. Singh, P. Gegenwart, and R. Valentí, Models and materials for generalized Kitaev magnetism, J. Phys.: Condens. Matter **29**, 493002 (2017).

[23] T. Takayama, A. Kato, R. Dinnebier, J. Nuss, H. Kono, L. S. I. Veiga, G. Fabbris, D. Haskel, and H. Takagi, Hyperhoneycomb iridate β-Li_2IrO_3 as a platform for Kitaev magnetism, Phys. Rev. Lett. **114**, 077202 (2015).

[24] A. Banerjee, J. Yan, J. Knolle, C. A. Bridges, M. B. Stone, M. D. Lumsden, D. G. Mandrus, D. A. Tennant, R. Moessner, and S. E. Nagler, Neutron scattering in the proximate quantum spin liquid $RuCl_3$, Science **356**, 1055 (2017).

[25] A. Glamazda, P. Lemmens, S.-H. Do, Y. S. Choi, and K.-Y. Choi, Raman spectroscopic signature of fractionalized excitations in the harmonic-honeycomb iridates β- and γ-Li_2IrO_3, Nat. Commun. **7**, 12286 (2016).

[26] L. J. Sandilands, Y. Tian, K. W. Plumb, Y.-J. Kim, and K. S. Burch, Scattering continuum and possible fractionalized excitations in α-$RuCl_3$, Phys. Rev. Lett. **114**, 147201 (2015).

[27] S.-C. Zhang and J. Hu, A four-dimensional generalization of the quantum Hall effect, Science **294**, 823 (2001).

[28] R. Chen, X.-X. Yi, and B. Zhou, Four-dimensional topological Anderson insulator with an emergent second Chern number, Phys. Rev. B **108**, 085306 (2023).

[29] Z.-R. Liu, R. Chen, and B. Zhou, Four-dimensional Floquet topological insulator with an emergent second Chern number, Phys. Rev. B **109**, 125303 (2024).

[30] B. Lian and S.-C. Zhang, Weyl semimetal and topological phase transition in five dimensions, Phys. Rev. B **95**, 235106 (2017).

[31] B. Lian and S.-C. Zhang, Five-dimensional generalization of the topological Weyl semimetal, Phys. Rev. B **94**, 041105(R) (2016).

[32] H. M. Price, O. Zilberberg, T. Ozawa, I. Carusotto, and N. Goldman, Four-dimensional quantum Hall effect with ultracold atoms, Phys. Rev. Lett. **115**, 195303 (2015).

[33] D. Jukić and H. Buljan, Four-dimensional photonic lattices and discrete tesseract solitons, Phys. Rev. A **87**, 013814 (2013).

[34] T. Ozawa, H. M. Price, N. Goldman, O. Zilberberg, and I. Carusotto, Synthetic dimensions in integrated photonics: From optical isolation to four-dimensional quantum Hall physics, Phys. Rev. A **93**, 043827 (2016).

[35] Y. Wang, H. M. Price, B. Zhang, and Y. D. Chong, Circuit implementation of a four-dimensional topological insulator, Nat. Commun. **11**, 2356 (2020).

[36] R. Yu, Y. X. Zhao, and A. P. Schnyder, 4D spinless topological insulator in a periodic electric circuit, Natl. Sci. Rev. **7**, 1288 (2020).

[37] A. Panigrahi, P. Coleman, and A. Tsvelik, Analytic calculation of the vison gap in the Kitaev spin liquid, Phys. Rev. B **108**, 045151 (2023).

[38] J. Knolle, D. L. Kovrizhin, J. T. Chalker, and R. Moessner, Dynamics of fractionalization in quantum spin liquids, Phys. Rev. B **92**, 115127 (2015).

[39] J. Nasu, M. Udagawa, and Y. Motome, Thermal fractionalization of quantum spins in a Kitaev model: Temperature-linear specific heat and coherent transport of Majorana fermions, Phys. Rev. B **92**, 115122 (2015).

[40] F. J. Wegner, Duality in generalized Ising models and phase transitions without local order parameters, J. Math. Phys. **12**, 2259 (1971).

[41] E. Fradkin and S. H. Shenker, Phase diagrams of lattice gauge theories with Higgs fields, Phys. Rev. D **19**, 3682 (1979).

[42] H. Yao and D.-H. Lee, Fermionic magnons, non-Abelian spinons, and the spin quantum Hall effect from an exactly solvable spin-1/2 Kitaev model with Su(2) symmetry, Phys. Rev. Lett. **107**, 087205 (2011).

[43] P. Jordan and E. Wigner, Über das Paulische Äquivalenzverbot, Z. Phys. **47**, 631 (1928).

[44] J.-T. Jin, J.-J. Miao, and Y. Zhou, Lacing topological orders in two dimensions: Exactly solvable models for Kitaev's sixteenfold way, SciPost Phys. **14**, 087 (2023).

[45] X.-Y. Feng, G.-M. Zhang, and T. Xiang, Topological characterization of quantum phase transitions in a spin-1/2 model, Phys. Rev. Lett. **98**, 087204 (2007).

[46] H.-D. Chen and Z. Nussinov, Exact results of the Kitaev model on a hexagonal lattice: spin states, string and brane correlators, and anyonic excitations, J. Phys. A: Math. Theor. **41**, 075001 (2008).

[47] F. D. M. Haldane, Model for a quantum Hall effect without Landau levels: Condensed-matter realization of the "parity anomaly", Phys. Rev. Lett. **61**, 2015 (1988).

[48] S. Chulliparambil, U. F. P. Seifert, M. Vojta, L. Janssen, and H.-H. Tu, Microscopic models for Kitaev's sixteenfold way of anyon theories, Phys. Rev. B **102**, 201111 (2020).

[49] P.-J. Chen and P. Coleman, Dataset for "a higher dimensional generalization of the Kitaev spin liquid, Zenodo (2026), https://doi.org/10.5281/zenodo.19199451.

[50] E. H. Lieb, Flux phase of the half-filled band, Phys. Rev. Lett. **73**, 2158 (1994).